



Extension of the double-ellipsoidal heat source model to narrow-groove and keyhole weld configurations



T.F. Flint^{a,b,**}, J.A. Francis^{b,*}, M.C. Smith^{a,b}, J. Balakrishnan^b

^a Modelling and Simulation Centre, The University of Manchester, Oxford Road, Manchester, UK

^b School of MACE, The University of Manchester, Oxford Road, Manchester, UK

ARTICLE INFO

Article history:

Received 5 October 2016

Received in revised form 7 February 2017

Accepted 8 February 2017

Available online 14 March 2017

Keywords:

Arc welding

Computational weld mechanics

Electron beam welding

Power density model

Heat transfer

Thermal analysis

ABSTRACT

The double-ellipsoidal heat power density model proposed by Goldak, has been widely used as the basis for modelling heat transfer in arc welding operations for more than thirty years. This approach has proved to be extremely effective for a wide range of arc welding operations. However, the application of a double-ellipsoidal heat power density distribution is less appropriate for keyhole-laser or electron-beam welding operations, or in situations where arc welding takes place within deep narrow grooves. In this paper the double-ellipsoidal distribution is extended to a double-ellipsoidal-conical heat power density model in order to accurately describe transient temperature fields for a wider range of geometries and welding processes. The new extended model was validated through comparing predicted welding thermal cycles with those measured for a single pass electron beam weld, as well as those measured in a multi-pass narrow groove gas-tungsten-arc weld. In both cases, excellent agreement was obtained between predicted and measured thermal transients.

© 2017 The Author(s). Published by Elsevier B.V. This is an open access article under the CC BY license (<http://creativecommons.org/licenses/by/4.0/>).

1. Introduction

Fusion welding is the most common method for assembling large metallic structures. Fusion welding involves the use of a concentrated heat source to bring about localised melting in order to join components. This localised heating leads to the generation of steep temperature gradients and rapid thermal transients, which in turn lead to large variations in micro-structure and mechanical properties, and to the generation of substantial levels of residual stress.

In the case of safety-critical components, such as those that arise in nuclear, power generation, offshore and in related sectors, it is critical that residual stresses are quantified with a high level of confidence. In order for a residual stress prediction to be made, an accurate thermal history must be obtained or predicted for the component, as was discussed by Radaj (1992). Given that many safety-critical components will have complex geometries and/or processing histories, such quantification is often contingent on the application of numerical models. Goldak et al. (1984) describe how

the accuracy of numerical predictions for transient thermal fields will in turn hinge on an accurate description of the welding heat source.

Rosenthal (1941) first applied Fourier's law to moving heat sources, which were represented as either point, line or plane sources of heat. This approach resulted in reasonable predictions for transient temperature fields at some distance from the heat source, but predictions were less accurate in the vicinity of the fusion zone. Subsequent developments were proposed by other researchers and these led to improved near-field predictions for conventional arc welds. Pavelic et al. (1969) made improvements by representing the welding arc as a distributed surface flux. In order to account for the effects of arc pressure and weld pool depression discussed by Friedman (1978), the heat source may be represented as a volumetric distribution.

An approach to representing welding heat sources, that was first proposed by Goldak et al. (1984), has been widely adopted by analysts over the past thirty years. Goldak and co-workers proposed a non-axisymmetric heat source distributed in three dimensions in order to better account for the depression of the weld pool surface owing to the arc pressure. One representation that was presented was based on a double-ellipsoidal heat power density distribution. However, Goldak et al. (1985) also pointed out that arbitrary functions can be utilised to define a distribution of heat flux on the surface of a weld, or a power density distribution throughout the

* Corresponding author.

** Principal corresponding author.

E-mail addresses: Thomas.Flint@manchester.ac.uk (T.F. Flint), John.Francis@manchester.ac.uk (J.A. Francis).

volume of a weld, and that these different functional distributions may be used with increasing or decreasing success depending on the parity of the distribution with the physical reality of the welding heat source. Goldak and co-workers stressed that if one has an exact solution of the temperature-enthalpy field in the weld pool, then one need only prescribe this solution to be a Dirichlet boundary condition, and the associated flux and power density distribution is the Lagrange multiplier that enforces this exact solution. Furthermore, appropriate flux and power density distributions must exist in cases where the temperature field solution exists. The only caveat on the choice of distribution function is that the integral must be unity. The approach proposed by Goldak has proved to be extremely effective at describing the arc as a heat source in a wide variety of applications, ranging from the case of an electric arc impinging on a flat plate, but also for cases where the arc is introduced to the base of a weld groove as described by both Bibby et al. (1985) and Gery et al. (2005).

In the time since the Goldak model was first published, there has been an increase in the application of narrow-groove arc welding process variants, which generally involve the preparation of deep and narrow weld grooves for welding thick sections of material. This increase has been driven by the desire to reduce the volumes of filler material that need to be deposited, thereby reducing joint completion times. Similarly, the utilisation of keyhole welding techniques based on the laser and electron beam (EB) welding processes has also increased. The mechanisms behind the keyhole formation in electron beam welding and the instabilities that may arise within the keyhole were reviewed by Sun and Karppi (1996). It is evident that the nature of arc welding in a deep and narrow groove, or keyhole welding with either an electron beam or a laser, is a very different scenario to that of an electric arc impinging on a flat plate. Thus, with the increasing utilisation of narrow-groove and keyhole weld configurations in mind, the authors felt compelled to examine the possibility of either extending an existing approach to the representation of welding heat sources, or proposing a new approach.

We begin by describing a double-ellipsoidal-conical heat power density model for welding heat sources; in which double-conical and double-ellipsoidal heat power density distributions, of similar form to those proposed by Bibby et al. (1985) and Goldak et al. (1984) respectively, are mathematically combined to create a power density distribution that is able to represent the heat source in a wider range of welding processes than previous power density distributions. We then describe the application of this heat source model to thermal analyses for the cases of a multipass narrow groove arc weld in a 30 mm thick SA508 steel plate, and a keyhole electron beam weld in a 30 mm thick SA508 steel plate. The performance of the model is then assessed based on a comparison of predicted thermal transients with those measured using thermocouples attached to the weld test pieces. The performance of the proposed model is also compared with the predictions arising from the application of the Goldak heat source model, as implemented with a double-ellipsoidal heat power density distribution.

2. Double-ellipsoidal conical heat source model

According to Fourier's law, heat flow is related to the transient temperature field in the domain. The temperature, $T(x, y, z, t)$, as a function of spatial co-ordinates, (x, y, z) , and time, t , satisfies the heat equation at every point in the domain as shown in Eq. (1).

$$\rho c_p \frac{\partial T}{\partial t} - k \nabla^2 T = q \quad (1)$$

where ρ , c_p and k are the mass density, specific heat capacity at constant pressure and the thermal conductivity respectively; $q_{(x,y,z,t)}$ is the rate of internal heat generation which represents the heat

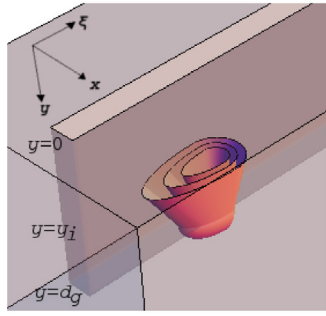
source or sink rate in the domain. Typically $q_{(x,y,z,t)}$ has been represented by a non-axisymmetric heat source as proposed by Goldak et al. (1984), typically a double-ellipsoidal heat power density distribution, for the case of arc welding, and by a three dimensional conical distribution for beam welding processes and plasma arc welding.

The double-ellipsoidal heat source has been shown to accurately represent the heat power density from an electric arc traversing across the surface of a flat plate. However, in cases where the weld configuration deviates significantly from an arc impinging on a flat plate, this distribution should be modified in order to account for heat transfer by convection and radiation to the walls of deep and narrow grooves. In the gas-tungsten arc welding (GTAW) process, for example, the gas shielding enables significant quantities of heat to be transported to the walls of the groove by forced convection and, as there is no fusible flux concealing the arc, by radiation transfer.

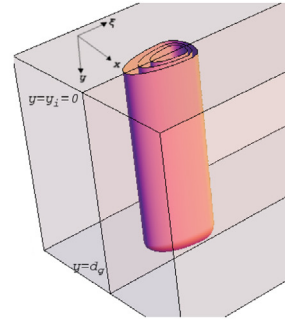
Consider a gas-tungsten electric arc traversing across the surface of a flat plate. For given welding conditions, there will be a distance, perpendicular to the welding line, over which the heat flux will decay to a fraction (say 5%) of its peak value. If the same gas-tungsten arc were now transposed to the base of a narrow groove this distance would necessarily change, since some portion of the arc energy would now be transferred directly to material located above the base of the groove, through mechanisms such as radiation and forced convection. Clearly such transfer would not occur in the case of a flat plate as no material would be located to either side of the electric arc. This heat decay as a function of distance from the weld line must then be related to the geometry of the groove.

In the proposed model, below the base of the groove the power density obeys the verified double-ellipsoidal distribution proposed by Goldak and decreases to a given fraction of the peak power in a Gaussian manner in three dimensions. Above the base of the groove, the distance over which the power density decreases by a given fraction is related to the bevel angle applicable to the wall of the groove. Therefore, above the base of the groove, surfaces of constant power density look like conical sections with different semi-major axes fore and aft of the arc location. In contrast, below the base of the groove, surfaces of constant power density lie on double-ellipsoids with different semi-major axes fore and aft of the arc location. These surfaces of constant power density are shown, for cases of an arc and electron beam weld, in Fig. 1a and b respectively.

For an electron beam incident on a flat surface the heat flux distribution is analogous to that of an arc at the base of a narrow groove. The focusing of the electron beam results in a Gaussian distribution of electron energies incident upon the domain surface. These electrons rapidly transfer their kinetic energy to the work-piece via scattering interactions, and toward the centre of the beam the electron energies may be sufficient to vaporise the base material. The resulting vapour pressure can displace molten metal, enabling subsequent electrons to travel further into the material. Toward the periphery of the beam, electrons will tend to have lower energies, and fewer collisions will be required in order for their energy to be transferred to the work-piece. Therefore, as the beam penetrates the domain, the effective radius of the Gaussian energy distribution decreases as the kinetic energy of the electrons therein is converted to thermal energy. There will also be some transfer of energy from the beam axis toward the beam periphery and, as such, the electron energies on the beam axis will gradually decay with increasing depth of penetration. This gradual decay in electron energies will determine the penetration depth since, at some point, the electron energies will no longer be sufficient to cause vaporisation of the molten metal. At this position on the beam axis, the heat ought to be deposited to the work-piece in a Gaussian manner from the end point of the beam in the domain. Therefore, above this position on the beam axis, surfaces of constant power density again



(a) A representation of the DEC heat source traversing along the base of a narrow groove welding geometry.



(b) A representation of the DEC heat source model used to model the electron beam process

Fig. 1. Representations of the DEC heat source model for an electric arc at the base of a narrow groove (a) and for an electron beam incident at the surface of a conducting domain (b). The parameters y_i and d_g are shown; y_i represents the initiation location of the heat source model in the y -dimension and d_g represents the transition plane between conical and ellipsoidal regions of the distribution.

lie on conical sections, and below this position surfaces of constant power density lie on appended ellipsoids as shown in Fig. 1b.

The heat sources in the GTAW and EB processes may be represented by the same model; one in which regions of constant power density lie on surfaces as shown in Fig. 1a and b. The Goldak heat source model is often employed with two appended ellipsoids, one leading and one trailing the axis of the heat source and, in general, different parameters are applied to each ellipsoid. The same approach has been preserved for the model proposed in this work.

A heat source model divided, as has been discussed, into two quadrants in the depth direction, and again into two quadrants in the direction of travel is therefore divided into four quadrants. In order to find the mathematical form of the distribution consider a Cartesian domain (z, y, ξ) separated into four quadrants by planes at $y = d_g$ and $\xi = 0$. The $y = d_g$ plane is analogous to the base of the groove in the arc welding analysis and to the termination point of the keyhole in the case of EB welding analysis. The point $y = y_i$ is set to correspond with the arc initiation point, in the vicinity of the tip of the tungsten electrode in GTAW and is used as an integration limit during the derivation of the heat source model. The locations of the $y = d_g$ and $y = y_i$ planes are shown in Fig. 2.

The transformation relating the fixed (x, y, z) and the moving (x, y, ξ) co-ordinate system is $\xi = z - vt$ where v is the velocity of the welding torch or electron beam source. The full derivation of the heat source model is outlined in Appendix A. For the region $y \geq d_g$, i.e. below the base of the groove in the arc welding case, the distribution is double-ellipsoidal. For the region $y_i \leq y \leq d_g$ the distribution is double-conical. The input voltage, current and heat transfer efficiency from the arc to the work-piece are represented by V, I and η respectively. The heat power density, in W m^{-3} , for any point within the domain is then given by Eq. (2).

It must be noted that, if the DEC heat source be applied in a numerical simulation where some portion of the heat source resides outside the numerical domain, then the integral of the heat power density over all integration points in the mesh will yield a value of the total heat input which is less than the applied total heat. In this case the proportion of the heat source that is immersed in the substrate material needs to be accounted for in the numerical analyses. In this work, this effect is accounted for by distinguishing between the true heat source power, Q , and the apparent heat source power, Q^* . The true heat source power will be familiar to many researchers and is given by $Q = \eta VI$, where η is the process efficiency, V is the welding voltage and I is the welding current. In the case of EB welding the product of voltage and current can simply be replaced by the beam power. In contrast, the apparent heat source power, Q^* , is given by $Q^* = Q/S = VI\eta/S$, where S is a shape factor

that represents the proportion of the proposed heat source that is immersed in the computational domain. Thus, the shape factor simply serves to correct for the fact that part of the heat source will not be generating heat because it resides outside the domain (i.e. the substrate material). In simple cases, such as for a full penetration electron beam weld, the heat source will be fully immersed in the substrate and the value of S will be unity. A shape factor approach has previously been used by other researchers and in commercial software such as the FEAT weld modelling tool software. The authors wish to emphasise that this approach to representing the heat source does not involve any arbitrary parameters. Four parameters are needed to determine Q^* , namely V, I, η and S . The first two are set by the operator during welding operations, while S is entirely determined by the weld groove and the heat source geometries, and η can be measured for a given welding process and compared with published values.

$$q = \frac{VI\eta}{S} \times \begin{cases} \frac{12\sqrt{3}R_{de}}{a c_r b \pi \sqrt{\pi}} e^{-3 \left(\left(\frac{x-b_g}{a} \right)^2 + \left(\frac{y-d_g}{b} \right)^2 + \left(\frac{\xi}{c_r} \right)^2 \right)} & \forall (y \geq d_g), (\xi \leq 0) \\ \frac{12\sqrt{3}R_{de}}{a c_f b \pi \sqrt{\pi}} e^{-3 \left(\left(\frac{x-b_g}{a} \right)^2 + \left(\frac{y-d_g}{b} \right)^2 + \left(\frac{\xi}{c_f} \right)^2 \right)} & \forall (y \geq d_g), (\xi \geq 0) \\ \frac{108e^3 R_{conical}}{\pi^2 (e^3 - 1) S_r (d_g - y_i)} e^{-3 \left(\left(\frac{\xi}{\Gamma_{c_r}} \right)^2 + \left(\frac{x-b_g}{\Gamma_a} \right)^2 \right)} & \forall (y \leq d_g), (\xi \leq 0) \\ \frac{108e^3 R_{conical}}{\pi^2 (e^3 - 1) S_f (d_g - y_i)} e^{-3 \left(\left(\frac{\xi}{\Gamma_{c_f}} \right)^2 + \left(\frac{x-b_g}{\Gamma_a} \right)^2 \right)} & \forall (y \leq d_g), (\xi \geq 0) \\ 0 & \forall (y < y_i) \end{cases} \quad (2)$$

where $\Gamma_a = a - ((a - a_i)((d_g - y)/(d_g - y_i)))$, $\Gamma_{c_r} = c_r - ((c_r - c_{r_i})((d_g - y)/(d_g - y_i)))$ and $\Gamma_{c_f} = c_f - ((c_f - c_{f_i})((d_g - y)/(d_g - y_i)))$. The fitting parameters; R_{de} , R_{de} , $R_{conical}$ and $R_{conical}$ are found by matching the power density distributions at the origin in the moving reference frame and are given in Eqs. (3)–(6) as:

$$R_{de} = \frac{1}{1 + \frac{c_f}{c_r} + \frac{(e^3 - 1)\sqrt{\frac{\pi}{3}} S_f (d_g - y_i)}{3 b c_r e^3 a} + \frac{(e^3 - 1)\sqrt{\frac{\pi}{3}} S_r (d_g - y_i)}{3 b c_r e^3 a}} \quad (3)$$

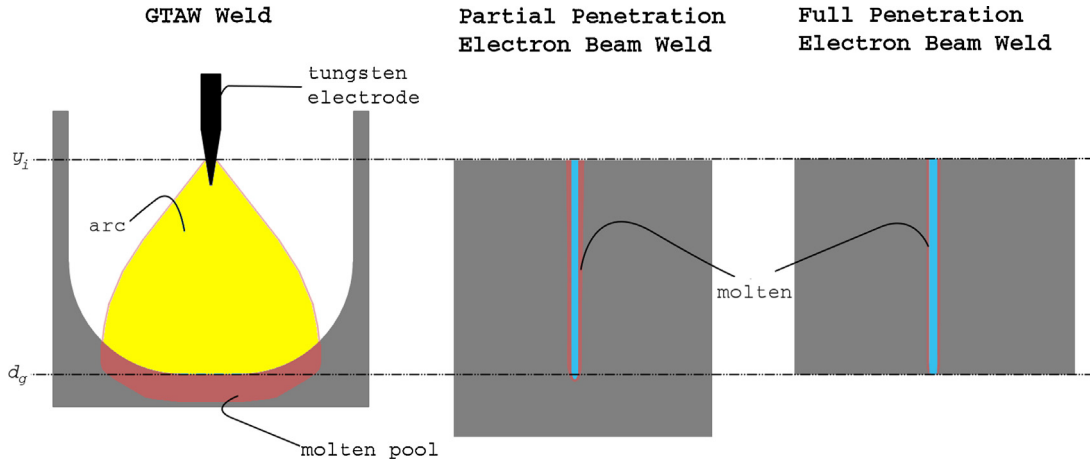


Fig. 2. Comparison between arc, partial penetration electron beam, and full penetration electron beam welding techniques.

$$R_{fde} = \frac{1}{1 + \frac{c_r}{c_f} + \frac{(e^3-1)\sqrt{\frac{\pi}{3}}S_f(d_g-y_i)}{3bc_f e^3 a} + \frac{(e^3-1)\sqrt{\frac{\pi}{3}}S_r(d_g-y_i)}{3bc_r e^3 a}} \quad (4)$$

$$R_{rconical} = \frac{1}{1 + \frac{S_r}{S_f} + \frac{3bc_f e^3 \sqrt{\frac{\pi}{3}} a}{(e^3-1)S_r(d_g-y_i)} + \frac{3bc_r e^3 \sqrt{\frac{\pi}{3}} a}{(e^3-1)S_r(d_g-y_i)}} \quad (5)$$

$$R_{fconical} = \frac{1}{1 + \frac{S_r}{S_f} + \frac{3bc_f e^3 \sqrt{\frac{\pi}{3}} a}{(e^3-1)S_f(d_g-y_i)} + \frac{3bc_r e^3 \sqrt{\frac{\pi}{3}} a}{(e^3-1)S_f(d_g-y_i)}} \quad (6)$$

with $S_r = c_r(2a + a_i) + c_{ri}(2a_i + a)$ and $S_f = c_f(2a + a_i) + c_{fi}(2a_i + a)$. A more complete explanation of the derivation of the DEC heat source model is provided in Appendix A. The parameters a , a_i , b , c_r , c_f , c_{ri} and c_{fi} are the heat power density parameters that determine the spatial gradient of the heat power density. The parameters a , b , c_r and c_f operate in the double-ellipsoidal portion of the power density distribution and are defined such that the power density falls to $0.05Q_{max}$ at these locations along their respective axes; a_i , c_{ri} and c_{fi} are defined such that the power density falls to $0.05Q_{max}$ at the $y=y_i$ plane following the approach of Goldak. The proposed heat source configuration is compared with the Goldak heat source, as implemented with a double-ellipsoidal heat power density distribution, in Fig. 3.

b_g is the location along the x axis where the power density reaches its maximum. The parameter b_g may itself be a function of time, $b_g(t)$, in the case where the welding heat source is weaved for better fusion. This leads to a power density distribution that looks like that pictured in Figs. 1a and 3. Examining the functional form of the heat source model it can be seen that as $d_g - y_i$ tends

to zero, the parameters $R_{rconical}$ and $R_{fconical}$ tend to zero and all the heat is present in the double-ellipsoidal component of the distribution. Similarly as the b parameter tends to zero R_{rde} and R_{fde} tend to zero and all the heat energy is deposited in the conical portion of the heat power density model. In the case of the EB process the values of the heat source parameters in their respective directions are closer; a to a_i , c_r to c_{ri} , and c_f to c_{fi} and so the heat power density distribution takes the form shown in Fig. 1b.

3. Validation of model

Validation of the DEC heat source model was performed by comparing measured thermal transients, obtained from a single pass full penetration EB weld and a 25 pass narrow groove GTA weld, with finite element predictions incorporating the DEC heat source. The experiments were performed on SA508 Grade 3 Class 1 steel parent material. This steel has industrial significance, as it is used to manufacture critical components in the primary circuit of pressurised water reactors, such as the reactor pressure vessel, steam generators and the pressuriser.

3.1. Gas tungsten arc welding

The GTAW process was performed on a SA508 Grade 3 Class 1 specimen 30 mm thick, 145 mm wide and 410 mm long with a groove machined along its length. The 15 mm wide groove was deep with respect to its width. The groove region was 240 mm long, with a 6 mm radius, a 1° groove angle and a 3 mm root face, as shown in Fig. 4. The specimen was instrumented with an array of

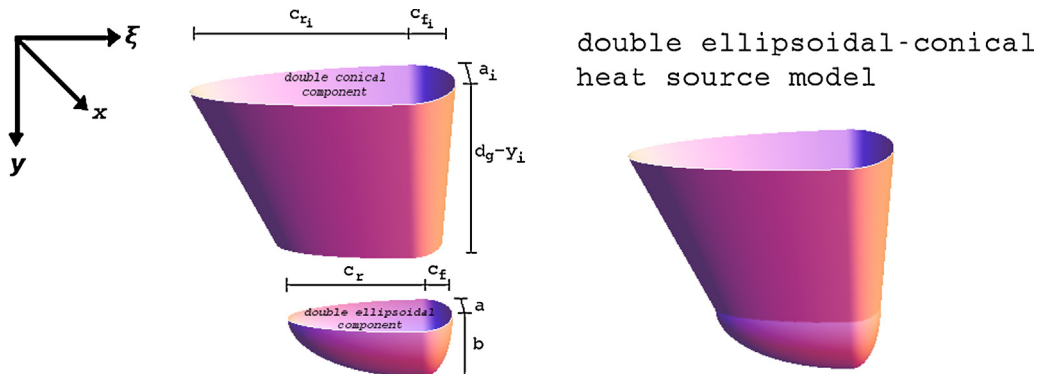


Fig. 3. Schematic diagram of DEC heat source model showing double-ellipsoidal and double-conical regions visualised as surfaces of constant power density.

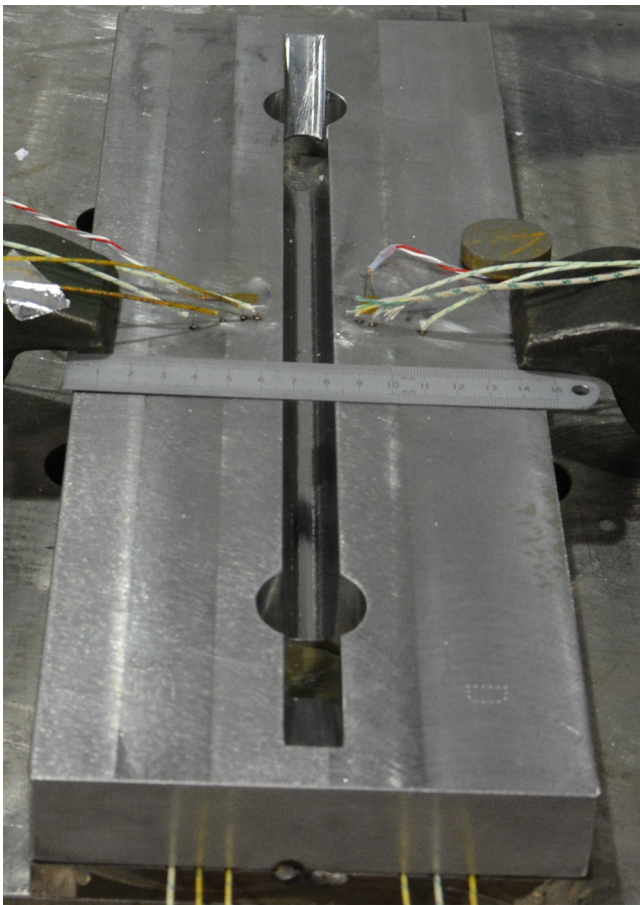


Fig. 4. Experimental set-up for the 25-pass GTAW weld before application of the electric arc.

thermocouples; a schematic diagram of the specimen and corresponding instrumentation is shown in Fig. 5.

A series of twenty five weld beads were deposited with SD31Ni1/4Mo filler wire. The average arc voltage and the travel speed for each pass were 11.2 V and 75 mm min⁻¹ respectively with an inter-pass temperature being maintained between 150 and 165 °C. Table 1 shows the welding current for passes 1–25. The chemical compositions for the SA508 steel and the filler wire are given in Table 2.



Fig. 6. Experimental set-up for the EB weld before application of the electron beam.

The electrode was weaved in the case of GTAW, and maintained at the boundary of the groove (± 7.5 mm from the centre of the groove) for 0.3 s before traversing to the opposite wall.

3.2. Electron beam welding

The joining of two plates, each 85 mm wide, 30 mm thick and 300 mm long to form a plate 170 mm wide was performed in a partial vacuum in the 2G position (i.e. with the beam horizontal) as shown in Fig. 6. The electron beam current and voltage were 90 mA and 150 kV respectively, and the beam traversed along the seam between the two plates at 200 mm min⁻¹. Fig. 6 shows the experimental set-up for the EB weld, and a schematic diagram of the instrumentation is given in Fig. 7.

3.3. Temperature measurement

Both specimens, i.e. for the GTAW and EB welds, were instrumented with k-type thermocouples. The thermocouples are effective at measuring temperatures in the range between -200 °C and 1350 °C. The sensitivity of the thermocouples is $\pm 0.004T$ where T is the temperature of the hot junction. The GTAW specimen was instrumented with twelve thermocouples in an array, at a position that was 205 mm along the welding axis, as shown in Fig. 5. The EB specimen was instrumented with eight thermocouples in an array, at a position that was 150 mm along the welding axis, as shown

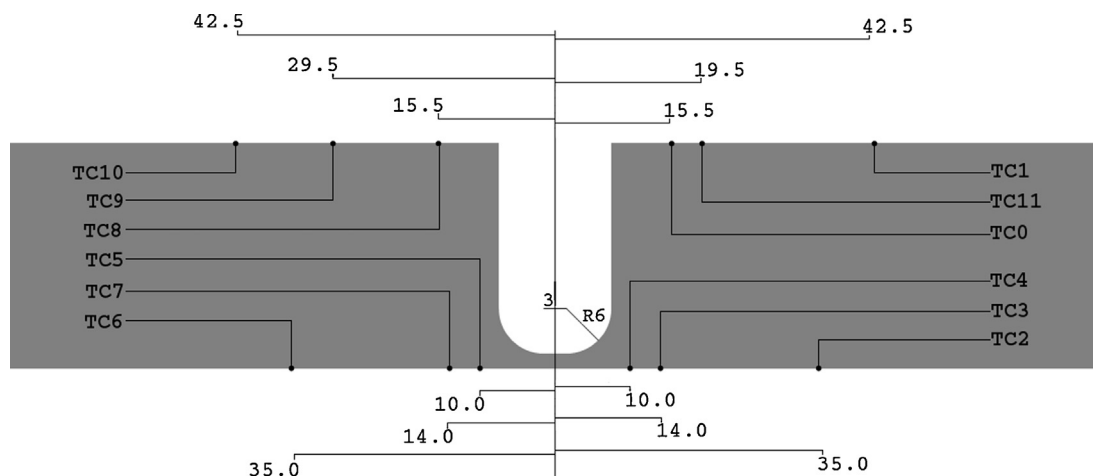


Fig. 5. Schematic diagram showing the cross section of the specimen at $z = 205$ mm. The groove geometry and thermocouple locations are visible. All dimensions are in mm.

Table 1

Welding currents for the 25 pass GTAW weld.

Weld (n)	1	2	3	4–7	8	9–14	15	16	17, 18	19, 20	21–25
Current (A)	175	190	220	275	300	325	350	375	325	350	325

Table 2

Chemical compositions of SA508 Grade 3 steel and filler wire (wt.%).

	C	Mn	Ni	Mo	Si	Cr	Co	Fe
SA508 parent	0.16	1.43	0.77	0.52	0.27	0.23	0.004	Bal.
Filler wire	0.10	1.47	0.88	0.25	0.20	0.03	0.004	Bal.

in Fig. 7. The data sampling rates for the GTAW and EB procedures were set at 5 Hz and 1 Hz respectively.

3.4. Metallography

Cuts were made, using electrical discharge machining (EDM), along the welding axis of the EB and GTAW specimens post-weld. The EDM sections were polished and etched in order to locate boundaries corresponding to the fusion zone (FZ) and heat affected zone (HAZ), and specifically the position corresponding to a peak temperature equal to the AC_1 temperature, in order to compare these with predictions made by simulations. The EDM sections were initially polished using 180 grade coarse grit SiC sheets. The grade of the polishing sheets was then increased to 400 grade, 600, 800 and 1200 fine grit abrasive sheets. The fine polishing was performed using abrasive cloths impregnated with diamond particles with sizes of 9 μm and 3 μm , respectively. 2% Nital solution was used to etch the specimens. This process revealed two distinct regions. The smaller of these regions exceeded the melting temperature for SA508 steel and is the fusion zone of the weld. At greater distances from the fusion boundary, the thermal cycle peak temperatures decrease progressively and more fine-grained structures are formed. Eventually the thermal cycle peak temperature decreases below the AC_1 temperature and the parent material structure is only tempered; the larger region visible in the macrographs separates the partially transformed inter-critical zone and the over-tempered regions in the HAZ as discussed by Alberry (1989). Francis et al. (2007) presented data for SA508 steel in their review article suggesting that the solidus and AC_1 temperatures are approximately 1500 °C and 700 °C respectively.

3.5. Modelling

The predicted thermal field was computed using the Abaqus finite element software. Three dimensional, transient, heat

transfer analyses were performed using 10 node quadratic tetrahedral (DC3D10) elements. The meshes produced to represent the GTAW and EB cases can be seen in Fig. 8a and b respectively. A small timestep in the order $\sim 10^{-2}$ s was chosen to ensure good temporal resolution in the simulation.

The DEC heat source model was implemented in a FORTRAN subroutine along with gap conductance and user defined field subroutines to appropriately activate the weld beads at the correct times to simulate the deposition of filler material at the heat source location. Temperature dependent thermal properties were used for the parent and filler materials. The latent heat capacity for SA508 steel was assumed to be the same as for similar steels in the literature, and was specified as $270 \times 10^3 \text{ J kg}^{-1}$ between the solidus and liquidus temperatures, which were taken to be 1500 °C and 1539 °C respectively.

3.5.1. GTAW modelling

In the finite element model for the GTAW process 176265 DC3D10 elements were used. The finite element mesh was graded such that more elements were present close to the welding path and within the weld beads, as can be seen in Fig. 8a. The simulation was divided into 25 steps, with the weld beads activated in their corresponding step, with material properties assigned appropriately using the user defined field subroutine. Convective and radiative heat losses, q_c and q_r , as described by Eqs. (7) and (8) respectively, were included from surfaces in the simulation domain, corresponding to surfaces in the experiments from which heat losses occurred.

$$q_c = h(T - T_0) \quad (7)$$

$$q_r = \varepsilon \sigma (T^4 - T_0^4) \quad (8)$$

The convective heat transfer coefficient, h , and the emissivity, ε , were found by investigating available literature and then fine tuning with cooling rates from thermocouple data and were found

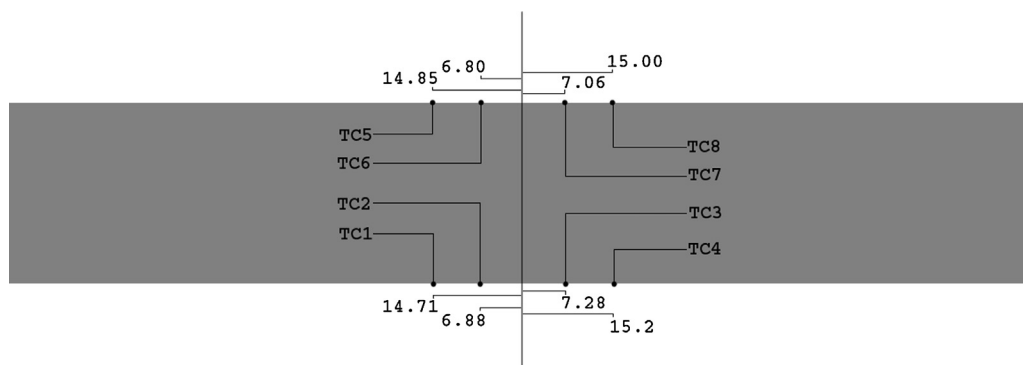


Fig. 7. Schematic diagram showing the cross section through the EB specimen at $z = 150$ mm; thermocouple locations are also visible. All dimensions are in mm.

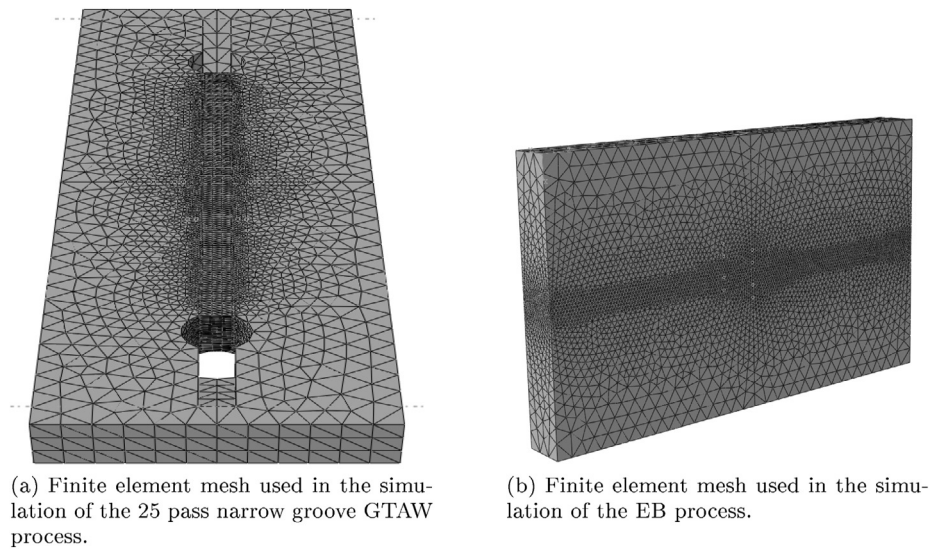


Fig. 8. Finite element discretised spatial domain used to model the narrow groove GTAW and EB welding processes. DC3D10 heat transfer elements were used in the simulation procedure.

to be $2 \times 10^{-6} \text{ W mm}^{-2} \text{ K}^{-1}$ and 0.6 respectively. Each process was simulated using both a double-ellipsoidal heat source model as well as the proposed DEC heat power density distribution.

Prior to fitting any heat source parameters an expression describing the weaving of the electrode in the GTAW weld was found using the information from the welding process, the pause time of the arc at the groove walls, and observations made during the experiment. A restricted sinusoidal function was used to model the b_g parameter after variables were found that set the time spent at peak deflection to the 0.3 s recorded in the experiment, as is shown in Fig. 9.

The first parameter that was found was the apparent efficiency term, η/S , that in the case of the DEC heat source, accounts for the heat transfer efficiency from the arc to the work-piece as well as the spatial extent of the heat source itself. The apparent efficiency term was found by matching the peak temperatures at thermocouples that were considered to be far enough from the welding torch to be insensitive both to the assumed heat source power density distribution and to positioning errors in regions of very high spatial thermal gradients. These also needed to be close enough to minimise the effects of convective heat loss from the plate and to record a sensible temperature rise. This selection procedure was straightforward for the single pass EB weld. However, it presented challenges in the case of multi-pass GTAW, where thermocouples had to be positioned so that they remained intact for all weld passes, and the varying distances from the weld torch required the use of multiple redundant arrays to record useable data for all passes.

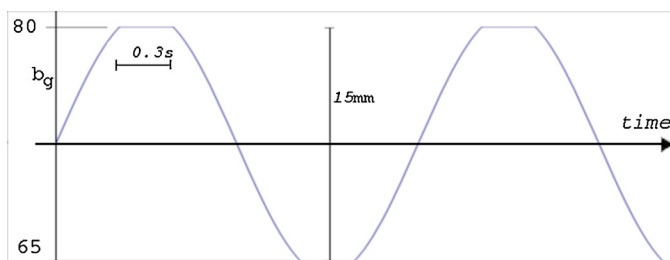


Fig. 9. Modified oscillatory function for simulating weave in the GTAW process; here the displacement in the x direction, b_g is plotted as a function of time.

For the remaining heat source parameters fitting was performed by initially, rather arbitrarily, setting the parameters in the welding axis c_r , c_{f_i} , c_f and c_{f_i} to values of 4, 6, 1 and 2 mm, respectively. The value of d_g was assumed to be the base of the groove (following the arguments stated in the model definition) for the first pass, 28 mm. The groove was filled over 25 passes, so it was assumed that each weld bead therefore was $(28/25)$ mm thick and for a given weld pass number, n , the value of d_g was given by $28 - (28/25)n$. The value of the y_i parameter with respect to d_g was then found by matching the predicted temperature rise with the experimentally measured temperature rise, for each weld pass, in two thermocouples. The closest thermocouples to the groove on the top and bottom of the specimen were chosen in order to fit the height of the conical portion, ensuring a representative distribution of heat with respect to measured experimental data. Once this had been performed it was noted that the groove geometry was such that the values of a and a_i should be similar, as the groove bevel angle is small. This fitting process involved several iterations before the final values of the parameters were obtained. The values of these parameters are shown in Table 3. The efficiency parameter for the double-ellipsoidal heat source was found by matching the far field thermocouple responses on the lower face of the plate to give the best fit further away from the heat source location. The thermocouple used to fit the efficiency was chosen such that at its location heat losses due to convection were small but the thermocouple was far enough from the weld pool that shape effects of the assumed power density distribution had decayed.

The apparent efficiency term, η/S , in the DEC heat source model is a combination of the true process efficiency, η , and geometric factors relating to the weld groove; a significant portion of the DEC heat source model is located in the free space of the weld groove and as such is required to be multiplied by a geometric factor, $1/S$, to arrive at the effective efficiency term used to simulate scenarios where a weld is performed at the base of a groove. If the entirety of the heat source model were present in the simulation domain, as is the case when simulating the electron beam weld, the geometric factor is, trivially, 1 and therefore the apparent efficiency is equal to the process efficiency. Therefore, when utilising the DEC heat source model to simulate a welding process at the base of a groove geometry, the apparent efficiency, η/S , may therefore be greater than unity. The volume integral of the heat source portion in free space could be performed in order to account for this if desired.

Table 3

Welding parameters used for the DEC heat source model and the double-ellipsoidal heat source model.

Pass		a	a_i	b	c_r	c_{r_i}	c_f	c_{f_i}	d_g
n	DEC	3.7	3.75	3.0	4.0	6.0	1.0	2.0	$28-(28/25)n$
	DE	3.8	–	2.5	4.0	–	1.5	–	$28-(28/25)n$

Table 4Welding pass number, fitted process efficiency, $d_g - y_i$, and calculated shape factor S for the 25 pass NG-GTAW process.

n	1	2	3	4	5	6	7	8	9	10
η	0.81	0.73	0.69	0.63	0.61	0.57	0.55	0.54	0.57	0.56
$d_g - y_i$	18.0	17.0	13.0	9.0	7.5	6.5	5.5	5.0	4.0	3.0
S	0.25	0.37	0.46	0.54	0.59	0.68	0.72	0.75	0.82	0.89

It should be noted that the process efficiency may be measured using calorimetry and the geometric factor in the numerical model may be found by summing, and time-averaging, the heat power density at the integration points of the numerical mesh. As such there is no loss in confidence in the model and the efficiency fitting procedure for the DEC model has the same generality as for the double-ellipsoidal model.

Table 4 shows the process efficiency, determined through temperature increases measured at the farthest thermocouples from the weld-region, as a function of weld-pass number. Table 4 also shows the shape factor, S , used in the simulation and the height of the conical component in the heat source model, $d_g - y_i$.

It is worth recognising at this stage that as the weld groove is filled and decreases in depth that the heat source representation tends to that of a double-ellipsoidal heat source; the height of the conical component reduces over the first 10 passes and the fitted process efficiency term tends to ~50% which is comparable to values used in simulations utilising the double-ellipsoidal heat power density distribution.

3.5.2. EB modelling

The finite element model representing the electron beam process contained 146374 DC3D10 elements. The finite element mesh was graded to incorporate more elements in the vicinity of the heat source as shown in Fig. 8b. The EB experiment was performed in a partial vacuum and so only radiation heat loss boundary conditions were applied, to all exposed faces, in the simulation. An emissivity value, ϵ , of 0.5 was found by matching the cooling rates of the thermocouple data to the simulated thermal response. The electron beam traversed along the length of the specimen at $x = 85$ mm, therefore the b_g parameter was set to 85 mm accordingly. The efficiency parameter for the EB process was found by matching the responses of thermocouples furthest from the joint. This yielded a fitted process efficiency of 58%. Once the efficiency had been found the heat source parameters could be fitted. The EB diameter used in the experiment was 2 mm, therefore the a_i parameter in the heat source model was set to this value. As the weld was a full penetration weld it was known that the value of a would be smaller than a_i but the magnitude would not be significantly different, a value of 1.75 mm was chosen. The value of the d_g parameter was initially set to be the depth of the plate, 30 mm, as the beam fully penetrated the domain. The initial parameters in the welding direction c_r , c_{r_i} , c_f , c_{f_i} and b were then set to values of 3, 4, 0.5, 2 and 0.01 mm respectively in order to iterate through heat source model configurations. This

fitting process required several iterations to find the best match with the thermocouple responses. Following these iterations it was found that the value of d_g gave a better fit to the thermocouples on the back of the plate if instead its value was set to 28.5 mm and the value of b was set to 3 mm. The final values of the heat source parameters used in the FE model are shown in Table 5, all units are in mm unless otherwise stated.

Lundbäck and Runnemalm (2005) noted that improved thermal results and the typical 'nail-head' fusion zone profile in the weld macro-graph are obtained when modelling EB processes if an additional surface heat component is summed to the through thickness heat source component. The effect of an additional surface heat component was investigated by summing a second DEC heat source with a considerably shorter length scale $d_{g2} - y_i$. In the simulation using two DEC heat sources the heat fraction in each heat source was allocated in proportion to the length scale; the same parameters were used for both DEC heat sources except the d_{g2} for the second DEC heat source was set to 0.6 mm, such that 2% of the heat input was present in the second DEC heat source. During the fitting of the DEC heat source parameters in the EB case it was found that this second DEC heat source had little effect on the thermocouple responses but it influenced the shape of the predicted solidus and AC₁ peak temperature isotherms near the surface of the plate where the beam entered, producing the familiar 'nail-head' cross section in the fusion zone.

4. Results

4.1. GTAW

The fitted heat source parameters for the narrow groove GTAW process are shown in Table 3. The fitted process efficiencies for the DEC and double-ellipsoidal heat source models are shown in Table 4; as are the geometric factors, S , and the height of the conical component of the DEC model for the various welding passes.

Fig. 10 shows the comparison between the experimental data during the third weld pass, and the thermal responses of the numerical model to the double-ellipsoidal and DEC heat source model, for the two thermocouples closest to the joint region.

Figure 11 shows the recorded increase in temperature for three representative thermocouples, together with the predicted temperature increases at these locations due to the DEC and double-ellipsoidal heat source models respectively, for the first nine weld passes.

Table 5

Welding parameters used for the DEC heat source model in the simulation of the EB process.

Parameter	a	a_i	b	c_r	c_{r_i}	c_f	c_{f_i}	η^a	d_{g1}	y_i
Value	1.5	2.0	3.0	4.0	4.0	1.0	2.5	0.58	29	0

^a Heat transfer efficiency is dimensionless.

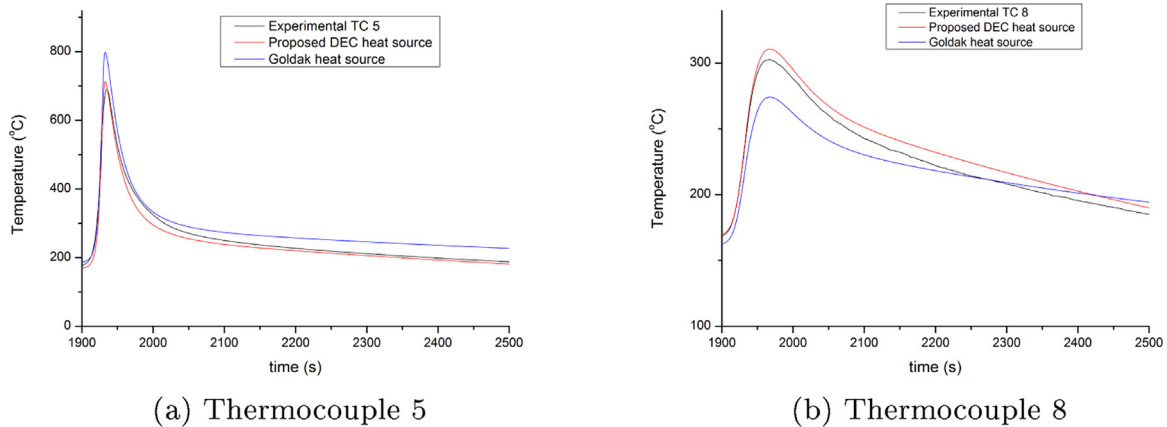


Fig. 10. Comparison between thermocouple data and predicted thermal responses for two thermocouples for pass 3 of the narrow groove GTAW process. These traces are representative of all passes.

It is clear from Fig. 11 that the DEC heat source model gives a more accurate temperature prediction, particularly for the thermocouples on the top-surface of the specimen, than the double-ellipsoidal model particularly for the initial weld passes where the welding geometry is particularly deep with respect to its width. The DEC heat source model has a more representative distribution of heat for the narrow-groove arc welding process and as such the predicted temperature responses for thermocouples located on the base and top-surface of the specimen are closer, than those generated with a double-ellipsoidal model, to those measured experimentally.

For the thermocouples farther away from the weld-line the effect of the different heat source is less pronounced, as one would expect, the spatial distribution of the heat source is averaged as the heat propagates over the larger distances. The fitted double-ellipsoidal heat source model under-predicts the temperature increase on the top face of the work-piece and greatly over-predicts the response on the lower face when the efficiency term is fitted with the far-field thermocouple data. Following the fitting of the heat source for the various passes the simulated solidus and AC_1 peak temperature isotherms were plotted in the finite element software. These predicted isotherms were overlaid on the polished macro-graph, as shown in Fig. 12, the white and magenta boundaries represent the solidus and AC_1 peak temperature isotherms respectively.

4.2. EB

Fig. 13 shows comparisons between the thermocouple data and numerically predicted thermal responses due to a single DEC heat source throughout the thickness of the computational domain as well as the thermal response due to this DEC heat source with an additional DEC heat source applied at the surface of the domain.

It can be seen that the addition of the second DEC heat source at the component surface where the electron beam enters the component has little effect on the thermal response at locations in the computational domain corresponding to the thermocouple locations. The only notable effect is the slight increase in the higher and lower temperatures recorded at the top and bottom surfaces of the computational domain respectively. This is to be expected as the addition of the surface component obviously alters the power density distribution and more heat is delivered into the top of the domain with respect to the case where a single DEC heat source was simulated. The greatest changes due to the addition of the surface source are associated with the slightly altered solidus and AC_1 peak temperature isotherms. Again, this is to be expected as the

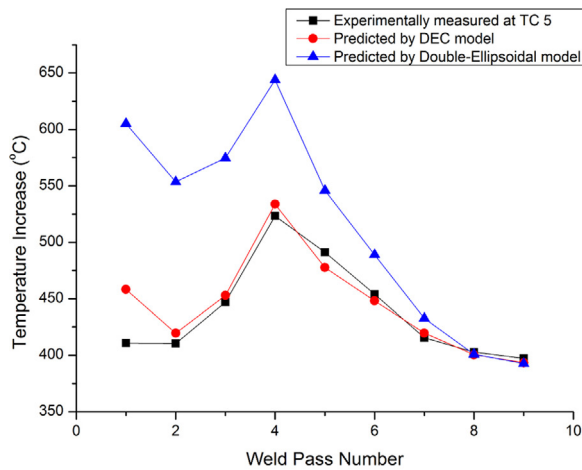
heat power density field incident on the computational domain has been slightly shifted and more heat has been allocated toward the surface than in the simulation where a single DEC heat source was applied. Fig. 14 shows the polished macro-graph for the EB specimen, with a visible FZ and HAZ, overlaid with the predicted AC_1 and fusion peak temperature isotherms (coloured in magenta and white respectively) for simulations utilising both a single DEC heat source two DEC heat sources where one heat source is considerably smaller in magnitude as discussed previously.

The simulated solidus and AC_1 peak temperature isotherms are closer to the experimentally observed ones for the case where the surface DEC source is added.

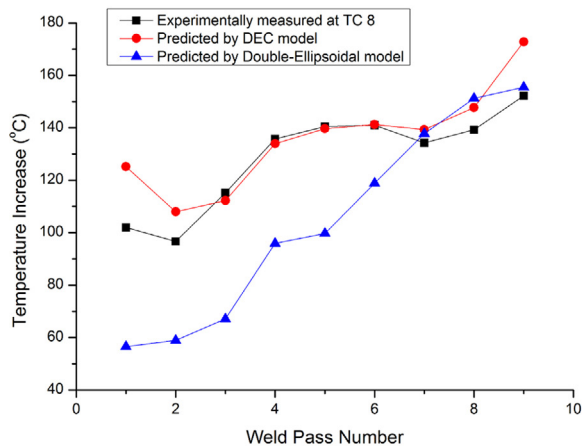
5. Discussion

The heat source model proposed in this work is a formal extension of the non-axisymmetric model proposed by Goldak et al. (1984), as implemented with a double-ellipsoidal heat power density distribution. As the parameter y_i tends to the value of d_g , the parameters $R_{rconical}$ and $R_{fconical}$ both tend to zero and the distribution collapses to be that of the double-ellipsoidal distribution. Similarly, as the parameter b tends to zero R_{rde} and R_{fde} tend to zero and the distribution tends towards a double-conical distribution. The mathematics also holds such that the integration over all space always remains unity; this tendency for the DEC power density model to approach the familiar double-ellipsoidal and double conical heat power density models will reassure researchers and provide confidence in the model. The double-ellipsoidal distribution is a special case of the double-ellipsoidal-conical distribution derived in this work. This parity is convenient and has the added benefit that Goldak's model, as implemented with a double-ellipsoidal heat power density distribution, has been heavily validated in both industrial and academic applications. Indeed it has been shown in this work that as the narrow groove is filled and its depth is no-longer large with respect to its width, the DEC heat source representation tends to that of the double-ellipsoidal model. However, in order for an accurate temperature prediction, especially in the first passes, the DEC heat source model should be utilised.

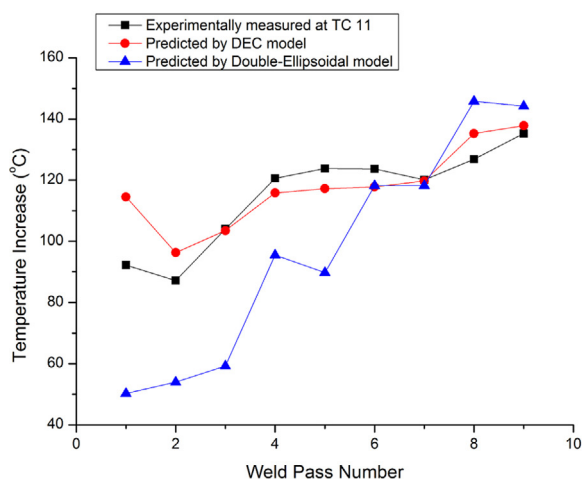
Representing the weld pool as a three dimensional distribution of heat has many advantages. However, the DEC model cannot predict the size and shape of the weld pool and heat affected zone alone. Spatial parameters in the model must be fitted to trusted data, usually in the form of measured weld pool dimensions, or predictions from a trusted computer model that accounts for physical phenomena in the weld pool such as fluid flow driven by surface-tension gradients as investigated by Heiple et al. (1983)



(a) Thermocouple 5



(b) Thermocouple 8



(c) Thermocouple 11

Fig. 11. Temperature increases recorded experimentally at three thermocouple locations along with those predicted by the proposed DEC heat source model and the double-ellipsoidal heat source model.

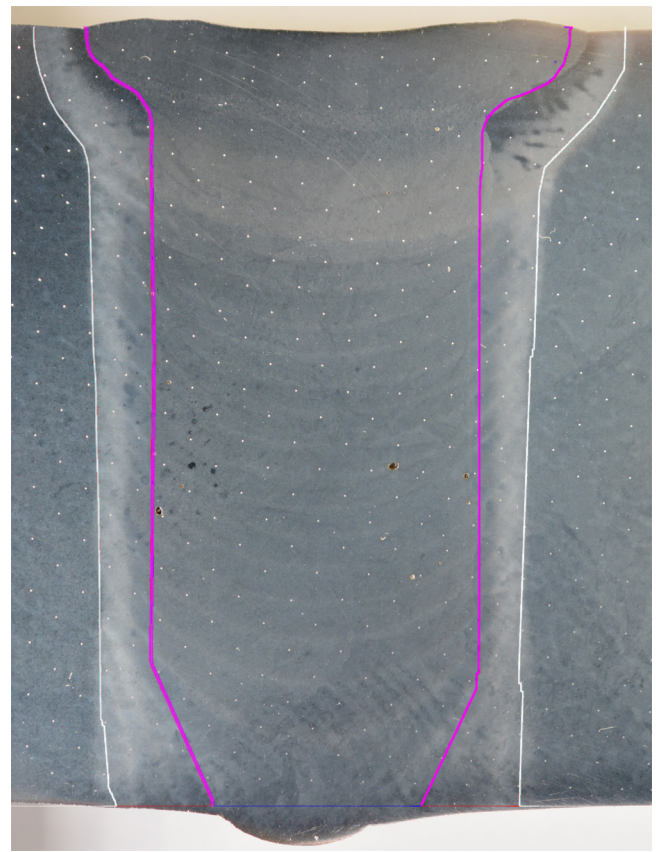


Fig. 12. Polished cross-section of the GTAW weld overlaid with simulated FZ and HAZ boundaries. For scaling purposes the thickness of the specimen is 30 mm. (For interpretation of the references to colour in this figure legend, the reader is referred to the web version of the article.)

or electromagnetic forces as discussed by Lancaster (1984). Sudnik et al. (1996) and Ohji and Nishiguchi (1988) have proposed hydrodynamic models of this type, which accurately predict the weld pool shape, and data from such models could readily be used to determine the spatial parameters for the DEC model.

In the electron beam welding case the portion of the heat source from d_g to $d_g + b$ had little effect as a considerable portion of the beam energy was lost out of the back of the component as the beam exited. Had the beam power been ramped up or only partially penetrated the domain, the effect of this portion of the heat source would have been more evident. This is an area for further investigation.

The fitted values that were obtained for the process efficiency in the DEC model for the case of the narrow-groove GTAW specimen (Table 4) seem reasonable and this provides a degree of confidence in the model. Values close to 0.8 were observed in the initial passes and, while these are high, such values have been reported previously by Cantin and Francis (2005). One might expect the process efficiency to be high in the base of a narrow groove, owing to reductions in radiative and convective heat losses. The process efficiency reduces as further passes are deposited, and this could be attributed to increases in radiative and convective losses as the groove geometry becomes less stifling to these effects. It is also worth noting that weaving of the torch will lead to the re-melting of fused material and this will inevitably be associated with a reduction in the fitted process efficiency. The values for the fitted process efficiency in the case of the EB weld are also comparable to published values by Vasileiou et al. (2015).

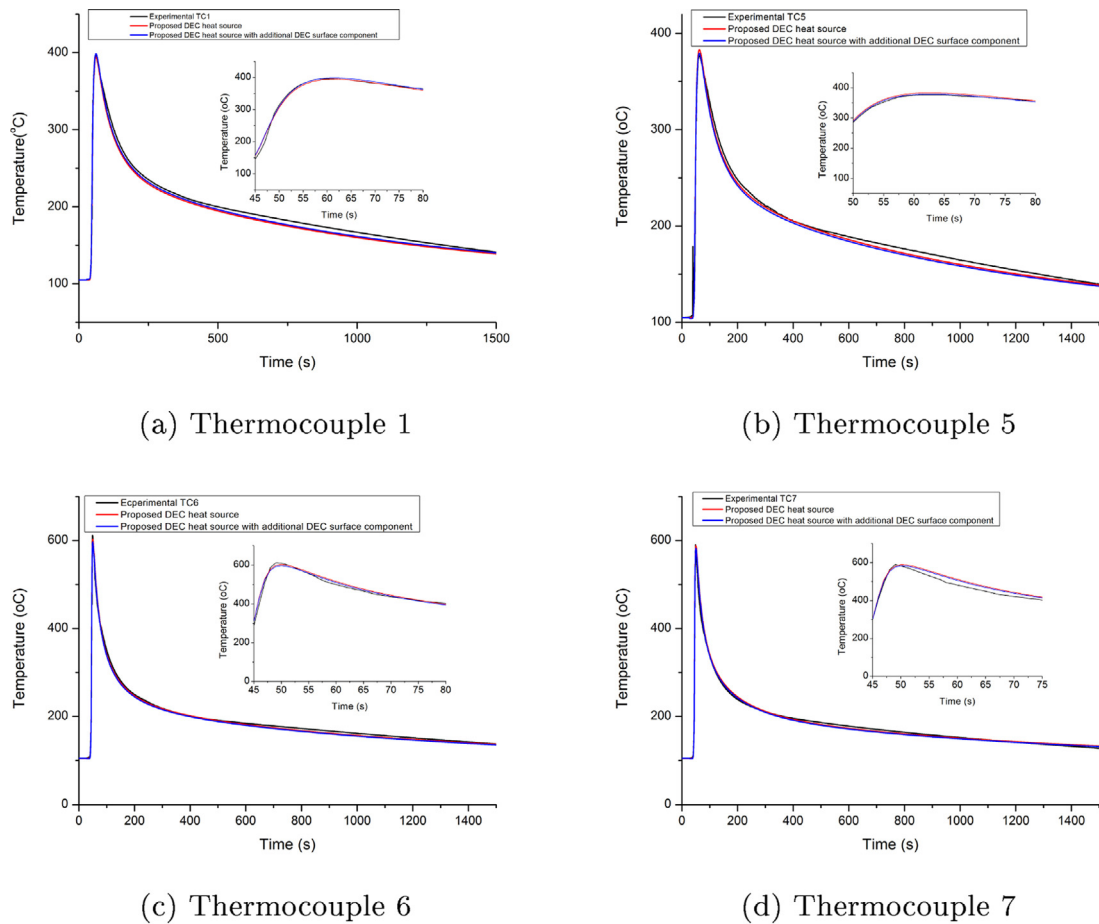


Fig. 13. Thermocouple data and simulated temperatures comparison for the EB process due to a single DEC heat source and with the addition of an extra surface DEC heat source with a 2% heat fraction; peak temperature regions are exploded.

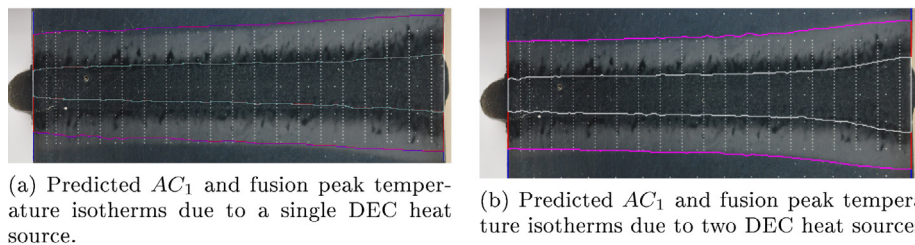


Fig. 14. Polished cross-section of the EB weld overlaid with simulated FZ and HAZ boundaries for a single DEC heat source and two DEC heat sources. (For interpretation of the references to colour in this figure legend, the reader is referred to the web version of the article.)

6. Conclusions

A double-ellipsoidal-conical (DEC) heat source has been developed and its performance has been assessed through comparing predicted thermal transients with those measured in experiments, through reference to both recorded thermocouple data and polished and etched macrograph sections extracted from weld test pieces. The proposed heat source model extends the model proposed by Goldak and co-workers, as implemented with a double-ellipsoidal heat power density distribution, in order to better represent heat transfer to the work piece for situations that involve welding in deep and narrow grooves, as well as for either partial-penetration or full-penetration welds in keyhole mode using high energy beams. The DEC model simplifies to the

double-ellipsoidal model for the case where a heat source is travelling along a flat surface. The DEC model has been validated through comparing predictions with measurements obtained from a single pass full-penetration electron beam weld and a multi-pass narrow groove gas-tungsten-arc weld.

When the DEC heat source model was used, the simulated thermal responses corresponding to thermocouple locations in the narrow groove GTA weld test piece were in excellent agreement with those measured experimentally. The predictions resulting from the DEC model were also significantly closer to the measured thermal responses when compared to predictions arising from the traditional double-ellipsoidal heat source model. As the weld groove was progressively filled, through the deposition of material during each weld pass, the DEC heat source distribution tended to

that of the well established double-ellipsoidal distribution, which is known to perform extremely well when welding on flat surfaces. This convergence was achieved through the conical component of the DEC heat source tending to zero. The DEC heat source was also shown to be extremely effective in the simulation of the electron beam weld – a weld configuration that is not amenable to modelling with a double-ellipsoidal heat source. Further improvements in predictions were achieved when a small surface power density was added, this surface component re-constructed the typical nail-head fusion zone cross section observed in electron beam welds.

In summary, the utility of the DEC heat source model proposed in this work is that it can cater for a wide range of weld configurations, ranging from a flat plate to a full-penetration keyhole weld. On this basis the authors believe it can serve as an effective heat source model for a wide range of weld configurations.

Acknowledgements

The authors wish to acknowledge financial support from the Engineering and Physical Sciences Research Council (EPSRC) through the NNUMAN programme grant in nuclear manufacturing (Grant No. EP/J021172/1). The authors also wish to thank Rolls-Royce for their support throughout the project; in particular Mr. Paul Hurrell for valuable discussions.

Appendix A. Derivation of DEC heat source model

Consider a Cartesian domain (x, y, ξ) separated into four quadrants by planes at $y = d_g$ and $\xi = 0$. In the leading ellipsoidal quadrant, $(y \geq d_g), (\xi \geq 0)$ the power density obeys a Gaussian distribution in three spatial dimensions with semi-major axes a, b, c_f in the x, y and z axes respectively as shown by Eq. (A.1). In the trailing ellipsoidal quadrant, $(y \geq d_g), (\xi \leq 0)$ the power density obeys a Gaussian distribution in three spatial dimensions with semi-major axes a, b, c_r in the x, y and z axes respectively as shown by Eq. (A.2). In conical quadrants of the power density distribution, $(y_i < y < d_g)$, the heat power density parameter governing the spatial decay rate in the depth distance is itself a function of depth. Therefore the leading and trailing conical quadrants are of the form stated by Eqs. (A.3) and (A.4) respectively.

$$q_{DE_f(x,y,\xi)} = Q_{0_{D_f}} e^{-3 \left(\left(\frac{x-b_g}{a} \right)^2 + \left(\frac{y-d_g}{b} \right)^2 + \left(\frac{\xi}{c_f} \right)^2 \right)} \quad \forall (y \geq d_g), (\xi \geq 0) \quad (A.1)$$

$$q_{DE_r(x,y,\xi)} = Q_{0_{D_r}} e^{-3 \left(\left(\frac{x-b_g}{a} \right)^2 + \left(\frac{y-d_g}{b} \right)^2 + \left(\frac{\xi}{c_r} \right)^2 \right)} \quad \forall (y \geq d_g), (\xi \leq 0) \quad (A.2)$$

$$q_{C_f(x,y,\xi)} = Q_{0_{C_f}} e^{-3 \left[\left(\frac{\xi^2}{\left(c_f - \left((c_f - c_{f_i}) \left(\frac{d_g - y}{d_g - y_i} \right) \right) \right)^2} \right) + \left(\frac{x^2}{\left(a - \left((a - a_i) \left(\frac{d_g - y}{d_g - y_i} \right) \right) \right)^2} \right) \right]} \quad \forall (y \leq d_g), (\xi \geq 0) \quad (A.3)$$

$$q_{C_r(x,y,\xi)} = Q_{0_{C_r}} e^{-3 \left[\left(\frac{\xi^2}{\left(c_r - \left((c_r - c_{r_i}) \left(\frac{d_g - y}{d_g - y_i} \right) \right) \right)^2} \right) + \left(\frac{x^2}{\left(a - \left((a - a_i) \left(\frac{d_g - y}{d_g - y_i} \right) \right) \right)^2} \right) \right]} \quad \forall (y \leq d_g), (\xi \leq 0) \quad (A.4)$$

In order to find the constants $Q_{0_{C_f}}, Q_{0_{C_r}}, Q_{0_{D_f}}$, and $Q_{0_{D_r}}$, which represent the maximum power density values in the frontal conical, rear conical, frontal ellipsoid and rear ellipsoidal quadrants of the DEC power density distribution respectively; we must integrate over the required spatial limits. It can be shown that:

$$\int_{-\infty}^0 \int_{y_i}^{d_g} \int_{-\infty}^0 q_{C_r} dx dy d\xi = \frac{\pi^2(e^3 - 1)(c_r(2a + a_i)c_{r_i}(a + 2a_i))(d_g - y_i)Q_{0_{C_r}}}{108e^3} = R_{r_{conical}} \quad (A.5)$$

Similar integrals were performed for all the quadrants of the power density distribution in order to find the Q_0 terms which represent the peak power density values of the distribution.

$$Q_{0_{C_f}} = \frac{108e^3 R_{f_{conical}}}{\pi^2(e^3 - 1)S_f(d_g - y_i)} \quad (A.6)$$

$$Q_{0_{C_r}} = \frac{108e^3 R_{r_{conical}}}{\pi^2(e^3 - 1)S_r(d_g - y_i)} \quad (A.7)$$

$$Q_{0_{D_f}} = \frac{12\sqrt{3}R_{f_{de}}}{ac_f b \pi \sqrt{\pi}} \quad (A.8)$$

$$Q_{0_{D_r}} = \frac{12\sqrt{3}R_{r_{de}}}{ac_r b \pi \sqrt{\pi}} \quad (A.9)$$

where $R_{f_{conical}}, R_{r_{conical}}, R_{f_{de}}$ and $R_{r_{de}}$ are matching expressions for the frontal conical, rear conical, frontal ellipsoid and rear ellipsoid portions of the power density distribution respectively that must be found in order to maintain power density continuity over the quadrant boundaries. The fitting parameters noted by $R_{r_{de}}, R_{f_{de}}, R_{r_{conical}}$ and $R_{f_{conical}}$ are found by matching the power density distributions at the origin in the reference frame of the moving heat source. In order to find the matching constant $R_{r_{de}}$, substitute $(x = b_g, y = d_g, \xi = 0)$ into the power density expression and sum the quadrants:

$$\left(R_{r_{de}} + \left(\frac{c_r R_{r_{de}}}{c_r} \right) + \left(\frac{6\sqrt{3}R_{r_{de}}}{ac_r b \pi \sqrt{\pi}} \frac{(c_r(2a + a_i) + c_{r_i}(a + 2a_i))(d_g - y_i)}{54e^3} \pi^2 (e^3 - 1) \right) + \left(\frac{6\sqrt{3}R_{r_{de}}}{ac_r b \pi \sqrt{\pi}} \frac{(c_f(2a + a_i) + c_{f_i}(a + 2a_i))(d_g - y_i)}{54e^3} \pi^2 (e^3 - 1) \right) \right) = 1 \quad (A.10)$$

After re-arranging the expression for the matching constant $R_{r_{de}}$, the expression can be shown to be:

$$R_{r_{de}} = \frac{1}{1 + \frac{c_f}{c_r} + \frac{(e^3 - 1)\sqrt{\frac{\pi}{3}}S_f(d_g - y_i)}{3bc_r e^3 a} + \frac{(e^3 - 1)\sqrt{\frac{\pi}{3}}S_r(d_g - y_i)}{3bc_r e^3 a}}$$

Similarly matching expressions $R_{f_{de}}, R_{r_{conical}}$ and $R_{f_{conical}}$ are found.

$$R_{f_{de}} = \frac{1}{1 + \frac{c_r}{c_f} + \frac{(e^3 - 1)\sqrt{\frac{\pi}{3}}S_f(d_g - y_i)}{3bc_f e^3 a} + \frac{(e^3 - 1)\sqrt{\frac{\pi}{3}}S_r(d_g - y_i)}{3bc_f e^3 a}}$$

$$R_{r_{conical}} = \frac{1}{1 + \frac{S_f}{S_r} + \frac{3bc_f e^3 \sqrt{\frac{3}{\pi}} a}{(e^3 - 1)S_r(d_g - y_i)} + \frac{3bc_r e^3 \sqrt{\frac{3}{\pi}} a}{(e^3 - 1)S_r(d_g - y_i)}}$$

$$R_{f_{conical}} = \frac{1}{1 + \frac{S_r}{S_f} + \frac{3bc_f e^3 \sqrt{\frac{3}{\pi}} a}{(e^3 - 1)S_f(d_g - y_i)} + \frac{3bc_r e^3 \sqrt{\frac{3}{\pi}} a}{(e^3 - 1)S_f(d_g - y_i)}}$$

Substituting the fitting expressions and (A.6), (A.7), (A.8) and (A.9), into (A.3), (A.4), (A.1) and (A.2), leads to the final form of the power density distribution expression:

$$q = \frac{VI\eta}{S} \times \begin{cases} \frac{12\sqrt{3}R_{de} e^{-3 \left(\left(\frac{x-b_g}{a} \right)^2 + \left(\frac{y-d_g}{b} \right)^2 + \left(\frac{\xi}{c_r} \right)^2 \right)}}{a c_r b \pi \sqrt{\pi}} & \forall (y \geq d_g), (\xi \leq 0) \\ \frac{12\sqrt{3}R_{de} e^{-3 \left(\left(\frac{x-b_g}{a} \right)^2 + \left(\frac{y-d_g}{b} \right)^2 + \left(\frac{\xi}{c_f} \right)^2 \right)}}{a c_f b \pi \sqrt{\pi}} & \forall (y \geq d_g), (\xi \geq 0) \\ \frac{108e^3 R_{r_{conical}} e^{-3 \left(\left(\frac{\xi}{\Gamma_{cr}} \right)^2 + \left(\frac{x-b_g}{\Gamma_a} \right)^2 \right)}}{\pi^2 (e^3 - 1) S_r (d_g - y_i)} & \forall (y \leq d_g), (\xi \leq 0) \\ \frac{108e^3 R_{f_{conical}} e^{-3 \left(\left(\frac{\xi}{\Gamma_{cf}} \right)^2 + \left(\frac{x-b_g}{\Gamma_a} \right)^2 \right)}}{\pi^2 (e^3 - 1) S_f (d_g - y_i)} & \forall (y \leq d_g), (\xi \geq 0) \end{cases}$$

where $\Gamma_a = a - ((a - a_i)((d_g - y)/(d_g - y_i)))$, $\Gamma_{cr} = c_r - ((c_r - c_{ri})((d_g - y)/(d_g - y_i)))$, $\Gamma_{cf} = c_f - ((c_f - c_{fi})((d_g - y)/(d_g - y_i)))$, $S_r = c_r(2a + a_i) + c_{ri}(2a_i + a)$ and $S_f = c_f(2a + a_i) + c_{fi}(2a_i + a)$.

References

- Alberly, P.J., 1989. Computer model for multipass repair welds in SA508 class 2 alloy. *Weld. J.* 68 (11), 442s–451s.
- Bibby, M.J., Goldak, J.A., Shing, G.Y., 1985. A model for predicting the fusion and heat-affected zone sizes of deep penetration welds. *Can. Metall. Q.* 24 (January (1)), 101–105.
- Francis, J.A., Bhadeshia, H.K.D.H., Withers, P.J., 2007. Welding residual stresses in ferritic power plant steels. *Mater. Sci. Technol.* 23 (September (9)), 1009–1020.
- Cantin, G.M.D., Francis, J.A., 2005. Arc power and efficiency in gas tungsten arc welding of aluminium. *Sci. Technol. Weld. Join.* 10 (April (2)), 200–210.
- Friedman, E., 1978. Analysis of weld puddle distortion and its effect on penetration. *Weld. J.* 57 (6), 161.
- Gery, D., Long, H., Maropoulos, P., 2005. Effects of welding speed, energy input and heat source distribution on temperature variations in butt joint welding. *J. Mater. Process. Technol.* 167 (August (2–3)), 393–401.
- Goldak, J.A., Bibby, M.J., Chakravarti, A., 1984. A new finite element model for welding heat sources. *Metall. Trans. B* 15, 299–305.
- Goldak, J.A., Patel, B., Bibby, M.J., Moore, J.E., 1985. Computational Weld Mechanics. Invited Opening Paper for AGARD Workshop – Structures and Materials 61st Panel Meeting., pp. 1–32.
- Heiple, C.R., Roper, J.R., Stagner, R.T., Aden, R.J., 1983. Surface active element effects on the shape of GTA, laser and electron beam welds. *Weld. J.* 62 (3), 72.
- Lancaster, J.F., 1984. The physics of welding. *Physics in Technology*, vol. 15., 2nd ed., pp. 73.
- Lundbäck, A., Runnemalm, H., 2005. Validation of three-dimensional finite element model for electron beam welding of Inconel 718. *Sci. Technol. Weld. Join.* 10 (6), 717–724.
- Ohji, T., Nishiguchi, K., 1988. Mathematical Modeling of Molten Pool in Arc Welding of Thin Plate. Springer Berlin Heidelberg, Berlin, Heidelberg.
- Pavelic, V., Tanbakuchi, R., Uyehara, O.A., Myers, P.S., 1969. Experimental and computed temperature histories in gas tungsten arc welding of thin plates. *Weld. J.* 48 (7), 295–305.
- Radaj, D., 1992. Heat Effects of Welding.
- Rosenthal, D., 1941. Mathematical theory of heat distribution during welding and cutting. *Weld. J.* 20 (5), 220–234.
- Sudnik, W., Radaj, D., Erofeev, W., 1996. Computerized simulation of laser beam welding, modelling and verification. *J. Phys. D: Appl. Phys.* 29, 2811–2817.
- Sun, Z., Karppi, R., 1996. The application of electron beam welding for the joining of dissimilar metals – an overview. *J. Mater. Process. Technol.* 59 (3), 257–267.
- Vasileiou, A.N., Smith, M.C., Jeyaganesh, B., Francis, J.A., Hamelin, C., 2015. The impact of transformation plasticity on the electron beam welding of thick-section ferritic steel components. In: 23rd International Conference on Structural Mechanics in Reactor Technology (SMiRT-23), p. 2014.